THE INFLUENCE OF ATMOSPHERIC DYNAMICS ON THE INFRARED SPECTRA AND LIGHT CURVES OF HOT JUPITERS

J. J. FORTNEY,[1,2,3] C. S. COOPER,[4] A. P. SHOWMAN,[4] M. S. MARLEY,[1] AND R. S. FREEDMAN[1,3]

ABSTRACT

We explore the infrared spectrum of a three-dimensional dynamical model of planet HD 209458b as a function of orbital phase. The dynamical model predicts dayside atmospheric pressure-temperature profiles that are much more isothermal at pressures less than 1 bar than one-dimensional radiative-convective models have found. The resulting dayside thermal spectra are very similar to a blackbody, and only weak water absorption features are seen at short wavelengths. The dayside emission is consequently in better agreement with ground-based and space-based secondary eclipse data than any previous models, which predict strong flux peaks and deep absorption features. At other orbital phases, absorption due to carbon monoxide and methane is also predicted. We compute the spectra under two treatments of atmospheric chemistry: one uses the predictions of equilibrium chemistry, and the other uses non-equilibrium chemistry, which ties the timescales of methane and carbon monoxide chemistry to dynamical timescales. As a function of orbital phase, we predict planet-to-star flux ratios for standard infrared bands and all *Spitzer Space Telescope* bands. In *Spitzer* bands, we predict two- to fifteenfold variation in planetary flux as a function of orbital phase with equilibrium chemistry, and two- to fourfold variation with nonequilibrium chemistry. Variation is generally more pronounced in bands from 3 to 10 μm than at longer wavelengths. The orbital phase of maximum thermal emission in infrared bands is 15–45 orbital degrees before the time of secondary eclipse. Changes in flux as a function of orbital phase for HD 209458b should be observable with *Spitzer*, given the previously achieved observational error bars.

Subject headings: binaries: eclipsing — planetary systems — radiative transfer — stars: individual (HD 209458)

1. INTRODUCTION

Astronomers and planetary scientists are just beginning to understand the atmospheres of the short-period giant planets known as "hot Jupiters" or "Pegasi planets." A key subset of these planets are those that transit the disk of their parent stars, which make them well suited for follow-up studies. The most well studied of these transiting hot Jupiters is the first to be discovered, HD 209458b (Charbonneau et al. 2000; Henry et al. 2000), a 0.69 M_J planet that orbits its Sun-like parent star at a distance of 0.045 AU.

Currently, considerable work on hot Jupiters is occurring on both the observational and theoretical fronts. In the past few years, several groups have computed dynamical atmosphere models for HD 209458b in an effort to understand the structure, winds, and temperature contrasts of the planet's atmosphere (Showman & Guillot 2002; Cho et al. 2003; Cooper & Showman 2005, 2006; Burkert et al. 2005). If the planet has been tidally de-spun and has become locked to its parent star, dynamical models are surely needed to understand the extent to which absorbed stellar energy is transported onto the planet's permanent night side. With the launch of the *Spitzer Space Telescope* , there is now a platform that is well suited for observations of the thermal emission from hot Jupiter planets.

Spitzer observations spanning the time of the planet's secondary eclipse (when the planet passes behind its parent star) have

been published for HD 209458b at 24 μm (Deming et al. 2005), TrES-1 at 4.5 and 8.0 μm (Charbonneau et al. 2005), and HD 189733b at 16 μm (Deming et al. 2006a). In all cases, the observed quantity is the planet-to-star flux ratio in *Spitzer* Infared Array Camera (IRAC), Infrared Spectrograph (IRS), or Multiband Imaging Photometer for *Spitzer* (MIPS) bands. The dual TrES-1 observations are especially interesting because they allow for a determination of the planet's mid-infrared spectral slope. Several efforts have also been made from the ground to observe the secondary eclipse of HD 209458b. Although no detections have been made, some important, occasionally overlooked upper limits at *K* and *L* band have been obtained. These include Richardson et al. (2003a) around 2.3 μm, Snellen (2005) in *K* band, and Deming et al. (2006b) at *L* band. These ground-based observations constrain the flux emitted by the planet in spectral bands where water vapor opacity is expected to be minimal; therefore, emitted flux should be high.

This influx of data has spurred a new generation of radiative-convective equilibrium models, whose resulting infrared spectra can be compared with data (Fortney et al. 2005, 2006; Burrows et al. 2005, 2006; Seager et al. 2005; Barman et al. 2005;). See Marley et al. (2006) and Charbonneau et al. (2006) for reviews. The majority of these models are one-dimensional. Authors weight the incident stellar flux by $\frac{1}{4}$, to simulate planetwide average conditions, or by $\frac{1}{2}$, to simulate dayside average conditions (with a cold night side). Barman et al. (2005) have investigated two-dimensional models with axial symmetry around the planet's substellar-antistellar axis and computed infrared spectra as a function of orbital phase. Iro et al. (2005) have extended one-dimensional models by adding heat transport due to a simple parameterization of winds to generate longitude-dependent temperature maps, but they did not compute disk-averaged spectra for these models. Very recently Burrows et al. (2006) have also investigated spectra and light

[1] Space Science and Astrobiology Division, NASA Ames Research Center, MS 245-3, Moffett Field, CA 94035; jfortney@arc.nasa.gov, mark.s.marley@nasa.gov, freedman@darkstar.arc.nasa.gov.
[2] Spitzer Fellow.
[3] SETI Institute, 515 North Whisman Road, Mountain View, CA 94043.
[4] Lunar and Planetary Laboratory and Department of Planetary Sciences, University of Arizona, Tucson, AZ, 85721; curtis@lpl.arizona.edu, showman@lpl.arizona.edu.

curves of planets with various day-night effective temperature differences, assuming one-dimensional profiles for each hemisphere. These one- and two-dimensional radiative-convective equilibrium models have had some success in matching *Spitzer* observations, but Seager et al. (2005) and Deming et al. (2006b) have shown that ground-based data for HD 209458b do not indicate prominent flux peaks at 2.3 and 3.8 μm, which solar composition models predict.

The various dynamical models for HD 209458b (Showman & Guillot 2002; Cho et al. 2003; Cooper & Showman 2005, 2006; Burkert et al. 2005) are quite varied in their treatment of the planet's atmosphere. We will not review them here, as that is not the focus of this paper. In general, temperature contrasts in the visible atmosphere are expected to be somewhere between 300 and 1000 K. What has been somewhat lacking for these dynamical models are clear observational signatures, which would in principle be testable with *Spitzer* or other telescopes. The purpose of this paper is to remedy that situation. Here we generate infrared spectra and light curves as a function of orbital phase for the Cooper & Showman (2006, hereafter, CS06) dynamical simulation. We present the first spectra generated for three-dimensional models of the atmosphere of HD 209458b.

2. METHODS

Here we take the first step toward understanding the effects of atmospheric dynamics on the infrared spectra of hot Jupiters. A consistent treatment of coupled atmospheric dynamics, non-equilibrium chemistry, and radiative transfer would be a considerable task. In a coupled scheme, given a three-dimensional *P-T* grid at a given time step, with corresponding chemical mixing ratios, the radiative transfer scheme would solve for the upward and downward fluxes in each layer. These fluxes would be wavelength dependent and would differ from layer to layer. The thermodynamical heating/cooling rate, which is the vertical divergence of the net flux, would then be calculated. The dynamics scheme would then use this heating rate, together with the velocities and *P-T* profiles in the grid at the previous time step, to a calculate the chemical abundances, velocities, and *P-T* profiles on the grid at the new time step. The process steps forward in time, as the radiative transfer solver again finds the new heating/cooling rates. The emergent spectrum of the planet could be found at any stage. In our work presented here, we performed a simplified calculation that contains some aspects of what will eventually be included in a fully consistent treatment.

2.1. *Dynamical Model*

Our input pressure-temperature (*P-T*) map is from CS06. As the dynamical simulations are described in depth in Cooper & Showman (2005) and CS06, we will only give an overview here. The CS06 model employs the ARIES/GEOS Dynamical Core, version 2 (AGDC2; Suarez & Takacs 1995). The AGDC2 solves the primitive equations of dynamical meteorology, which are the foundation of numerous climate and numerical weather prediction models (Holton 1992; Kalnay 2002). The primitive equations simplify the Navier-Stokes equations of fluid mechanics by assuming hydrostatic balance of each vertical column of atmosphere. Forcing is due to incident flux from the parent star, through a Newtonian radiative process described in CS06. The CS06 model is forced from the one-dimensional radiative-convective equilibrium profile of Iro et al. (2005), which assumes globally averaged planetary conditions.

For their simulations, CS06 take the top layer of the model to be 1 mbar. The model atmosphere spans ~15 pressure scale heights between the input top layer and the bottom boundary at 3 kbar.

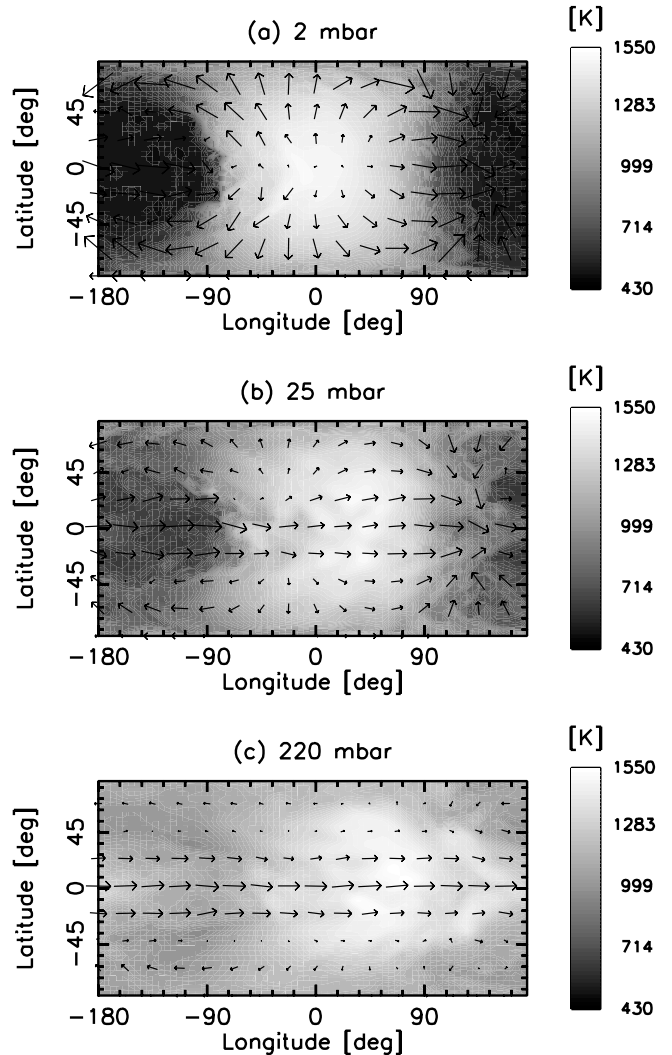Fig. 1.—Global temperature map at 2 mbar (*top panel*), 25 mbar (*middle panel*), and 220 mbar (*bottom panel*) for the CS06 dynamical simulation. Arrows show the direction and relative magnitudes of winds. Each longitude minor tick mark is 18°, and each latitude minor tick mark is 9°. Each panel uses the same temperature shading scheme.

CS06 use 40 layers evenly spaced in log pressure. A *P-T* profile is generated at locations evenly spaced in longitude (in 5° increments) and latitude (in 4° increments). The 72 longitude and 44 latitude points create 3168 *P-T* profiles. In Figure 1 we show the CS06 grid at three pressure levels, near ~2, 20, and 200 mbar. Previous work has shown these levels likely bracket the pressures of interest for forming mid-infrared spectra (Fortney et al. 2005). All three panels of Figure 1 use the same brightness scale for easy comparison between pressure levels.

At the 2 mbar level, where radiative time constants are short (Iro et al. 2005; Seager et al. 2005), the atmosphere responds quickly to incident radiation. Winds, although reaching a speed of up to 8 km s^{-1}, are not fast enough to lead to significant deviations from a static atmosphere, which implies that the hottest regions remain at the substellar point. The arrows indicate a wind pattern that attempts to carry energy radially away from the hot spot. At this pressure, the atmosphere somewhat resembles the two-dimensional radially symmetric static atmosphere of Barman et al. (2005), who found a hot spot at the substellar point and a uniformly decreasing temperature as radial distance from this point increased. The night side appears nearly uniform, and colder.

At the 25 mbar level, it is clear that a west-to-east circulation pattern has emerged at the equator, and the center of the planet's warm region has been blown downstream by $\sim 35°$. The wind from the west dominates over the predominantly radially outward wind seen at the 2 mbar level. Day-night temperature contrasts are not as large at this pressure as they are at 2 mbar.

At the 220 mbar level, the center of the hot spot has been blown downstream by $\sim 60°$. This jet extends from the equator to the midlatitudes; the gas in the jet is warmer than gas to the north or south. The radiative time constants become longer the deeper one goes into the atmosphere (Iro et al. 2005). Hence, winds are better able to redistribute energy, leading to weaker temperature contrasts, which cannot simply be characterized as "day-night."

2.2. Logistics and Radiative Transfer

Unlike other published models, we stress that the spectra generated here are from a dynamical atmosphere model that is *not* in radiative-convective equilibrium. Each of the 3168 *P-T* profiles from CS06 have, without modification (aside from interpolation onto a different pressure grid), been run through our radiative transfer solver. No iteration is done to achieve radiative equilibrium. The equation of radiative transfer is solved with the two-stream source function technique described in Toon et al. (1989). This is the same infrared radiative transfer scheme used in Fortney et al. (2005, 2006) and M. S. Marley et al. (2006, in preparation). We ignore contributions due to scattered stellar photons, as discussed below.

At a given orbital position, the CS06 map in longitude is remapped into an apparent longitude (as seen from Earth), while the latitude remains unchanged. See Figure 2 for a diagram. Here we ignore the $3°\!.4$ that the orbit differs from being exactly edge-on (Brown et al. 2001). At a given orbital angle φ—for each patch of the planet—the cosine of the angle θ from the subobserver point, μ, is calculated. This μ is consistently included when solving the radiative transfer, which means that the effects of limb darkening (or brightening) are automatically incorporated. We interpolate in a pressure-temperature-abundance grid (Lodders & Fegley 2002), such that any given point in the three-dimensional model has the atomic and molecular abundances that are consistent with that point's pressure and temperature.

At any given time, the one-half of the planet that is not visible is not included in the radiative transfer. The 1584 visible points, at which the emergent specific intensity (ergs s^{-1} cm^{-2} Hz^{-1} sr^{-1}) is calculated, are then weighted by the apparent visible area of their respective patches. These intensities are summed up to give the total emergent flux density (ergs s^{-1} cm^{-2} Hz^{-1}) from the planet. The spectra generated by the patch-by-patch version of the code were tested against spectra from one-dimensional gray atmospheres and our previously published hot Jupiter profiles.

Emergent spectra are calculated from 0.26 to 325 μm, but since we ignore the contribution due to scattered stellar flux, the spectra at the very shortest wavelengths have little meaning. However, for the radiative-equilibrium HD 209458b model published in Fortney et al. (2005) they found that scattered stellar flux is greater than thermal emission only at wavelengths less than ~ 0.68 μm. We expect that a considerable amount of "visible" light that may eventually be seen from hot Jupiters is due to thermal emission. We note that by 1 μm thermal emission is 100 times greater than scattered flux. Here we will present spectra for wavelengths from 1 to 30 μm.

We note that the radiative transfer at every point is solved in the plane-parallel approximation. While this treatment is sufficient for our purposes, we wish to point out two drawbacks. The first is that, near the limb of the planet, we will tend to overestimate the path lengths of photons emerging from the atmosphere, as the curvature
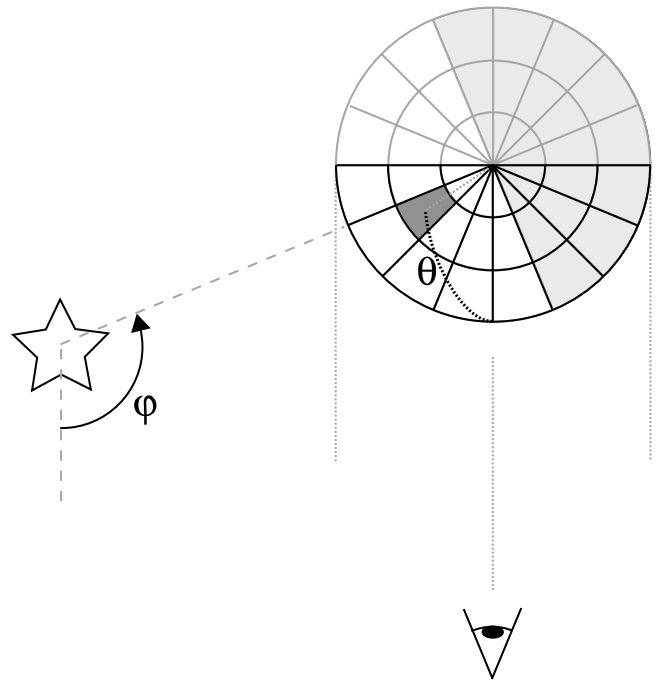

Fig. 2.— Top-view diagram of the planetary orbit. The CS06 latitude/longitude grid covers the entire planet. The planet's night side is shaded gray. At every angle in the orbit (φ), the longitude is remapped to give the apparent longitude and latitude, as viewed by the distant observer. The cosine of the angle θ made between a patch of the planet and the subobserver point is μ.

of the atmosphere is neglected. The second issue also occurs near the limb. We cannot treat photons whose path, in a completely correct treatment, would start in one column but emerge from an adjoining column. However, atmospheric properties in any two adjoining columns are in general quite similar. The former issue, that of the plane-parallel approximation, is likely more important, and should be addressed at a later time, when data precision warrants it. Here we note that in our tests 95% of planetary flux emerges from within 75° of the subobserver point, such that these limb effects will have little effect on the disk-summed spectra and light curves that we present.

When generating our model spectra, we use the elemental abundance data of Lodders (2003) and chemical equilibrium compositions computed with the CONDOR code, as described in Fegley & Lodders (1994), Lodders & Fegley (2002), and Lodders (2002). In § 2.3 we discuss deviations from equilibrium chemistry in the atmosphere of HD 209458b, as calculated by CS06. At this time, we ignore photochemistry, which has been shown by Visscher & Fegley (2006) to be reasonable at $P > 10$ mbar. For the most part, the infrared spectra of hot Jupiters are sensitive to opacity at $10 \lesssim P \lesssim 200$ mbar (Fortney et al. 2005), so equilibrium chemistry calculations are probably sufficient. As discussed in Fortney et al. (2006), we maintain a large and constantly updated opacity database, which is described in detail in R. S. Freedman & K. Lodders (2006, in preparation). The pressure, temperature, composition, and wavelength-dependent opacity is tabulated beforehand using the correlated-*k* method (Goody et al. 1989) in 196 wavelength interval bins. The resulting spectra are therefore of low resolution. However, low resolution is suitable for the task at hand, as we are interested in band-integrated fluxes and the radiative transfer must be solved at 1584 locations on the planet at many (here, 36) orbital phases.

In Williams et al. (2006), which focused on examining asymmetrical secondary eclipse light curves caused by dynamical

redistribution of flux, we investigated the effects of limb darkening for HD 209458b for the CS06 map. These effects are hard to disentangle from general brightness variations due to temperature differences generated by dynamics. Limb darkening in a particular wavelength would be manifested as a brightness temperature that decreases toward the limb relative to a brightness temperature map computed assuming normal incidence at every point. On the planet's day side, where the P-T profiles are somewhat isothermal, limb darkening is not expected to be significant. Indeed, only at angles greater than ∼80° from the subsolar point was dayside limb darkening as large as 100–200 K calculated. As noted, due to our plane-parallel approximation, this is likely to be somewhat of an overestimation.

2.3. *Clouds and Chemistry*

Before calculating spectra for this dynamic atmosphere, it is worthwhile to step back and look at the atmospheric P-T profiles with an eye toward understanding the effects that clouds and chemistry may have on the emergent spectra. In Figure 3 we plot a random sampling of the 3168 P-T profiles and compare them to cloud condensation and chemical equilibrium boundaries. It should be noted that there is a greater density of profiles on the left side of the plot. These are profiles from the relatively uniform and cool night hemisphere. Also of note is that at pressures less than ∼200 mbar, the warmer profiles are fairly isothermal, with quite shallow temperature gradients.

The CS06 profiles are nearly everywhere cooler than the condensation curves of iron and Mg-silicates. These clouds will form, but for these profiles, cloud bases would lie deep in the atmosphere at pressures greater than 1 kbar, as this is the highest pressure at which the profiles cross the condensation curves of these species. The opacity from such deep clouds would have *no effect* on the spectrum of HD 209458b.

The temperatures of the CS06 simulation are computed as departures from the equilibrium temperature profile of Iro et al. (2005) as described in CS06. If a warmer base profile had been selected, such as Fortney et al. (2005) or Barman et al. (2005) (which are 100–300 K warmer at our pressures of interest), these curves could be shifted to the right by 100°–300°. Marley et al. (2006) provide a graphical comparison of profiles computed by Iro et al. (2005) Fortney et al. (2005) and Barman et al. (2005) under similar assumptions concerning redistribution of stellar flux and atmospheric abundances; they find differences of up to 300 K at 100 mbar. These differences can probably be attributed to different opacity databases, molecular abundances, radiative transfer methods, and perhaps incident stellar fluxes. For the Fortney et al. (2005) profile, the major heating species are H_2O bands from 1 to 3 μm and neutral atomic Na and K, which absorb strongly in the optical. The major cooling species are CO, at 5 μm, and H_2O in bands at 3 and 4–10 μm, although for a colder profile, such as CS06 nightside profiles, CH_4 would also cool across these wavelengths. CS06 chose the Iro et al. (2005) profile because Iro et al. also computed atmospheric radiative time constants, which other authors have not done to date. Here, the computed nightside profiles cross the condensation curve of Na_2S at low pressure. Showman & Guillot (2002) and Iro et al. (2005) pointed out that the transit detection of weak neutral atomic Na absorption by Charbonneau et al. (2002) could be explained if a large fraction of Na was tied up in this condensate.

If the predictions of equilibrium chemistry hold for this atmosphere, then it would appear that at pressures up to 100 mbar, CH_4 would be the main carbon carrier on the planet's nightside, while CO would be the main carrier on the day side. This would
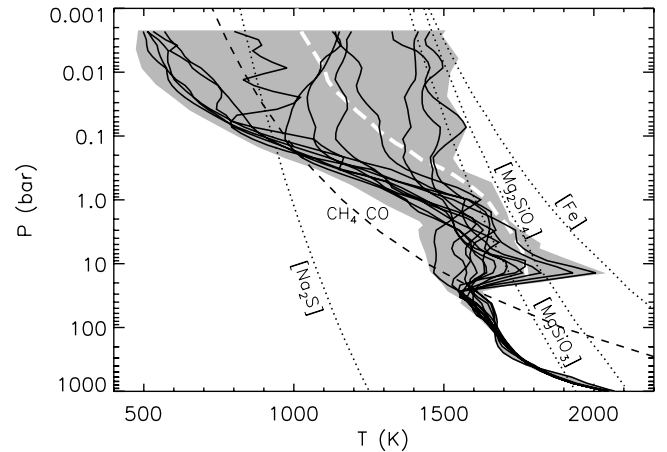

Fig. 3.—In gray is the full pressure and temperature extent of the 3168 P-T profiles from the CS06 simulation. In thick black are 13 randomly selected profiles that allow one to make out individual profile shapes and temperatures. In the middle of the gray, shown in white long dashes, is the Iro et al. (2005) profile. The labeled dotted curves show the condensation curves of important cloud species. The dashed curve shows where CH_4 and CO have an equal abundance. All of these boundaries assume solar abundances. Note that dayside and limb profiles tend to be generally isothermal at $P < 200$ mbar. The nightside profiles tend to plot over one another on the far left.

lead to dramatically different spectra for these hemispheres, especially at near-infrared and mid-infrared wavelengths.

However, equilibrium chemical abundances would be expected only if chemical timescales are faster than any mixing timescales. The relative abundances of CO and CH_4 can be driven out of equilibrium if mixing timescales due to dynamical winds are faster than the timescale for relaxation to equilibrium of the (net) reaction

$$CO + 3H_2 \leftrightarrow CH_4 + H_2O. \qquad (1)$$
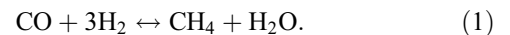
The time constant for chemical relaxation toward equilibrium is a strong function of temperature and pressure; it is short in the deep interior and extremely long in the observable atmosphere. Deviations from CH_4/CO equilibrium are due to the long timescale for conversion of CO to CH_4, and are well known in the atmospheres of the Jovian planets (Prinn & Barshay 1977; Fegley & Prinn 1985; Fegley & Lodders 1994; Bézard et al. 2002; Visscher & Fegley 2005) and brown dwarfs (Fegley & Lodders 1996; Noll et al. 1997; Griffith & Yelle 1999; Saumon et al. 2000, 2003, 2006), where vertical mixing can be due to convection and/or eddy diffusion. CS06 follow timescales for CH_4/CO chemistry taken from Yung et al. (1988) and find that vertical winds of 5–10 m s^{-1} push this system out of equilibrium at pressures of interest for the formation of infrared spectra. They find that the quench level, where the mixing timescale and chemistry timescale are equal, is ∼1–10 bar, which is below the visible atmosphere. Above this quench level, the mole fractions of CO and CH_4 are essentially constant. They find that the CH_4/CO ratio becomes homogenized at pressures less than 1 bar *everywhere* on the planet. For their nominal models this CH_4/CO ratio is ∼0.014, meaning that the majority of carbon is indeed in CO. However, a nonnegligible fraction of carbon remains in CH_4 on both the day and the night hemispheres. We note that CS06 ignore possible effects due to photochemistry on the CO and CH_4 mixing ratios. Given the few explorations into hot Jupiter carbon and oxygen photochemistry to date (Liang et al. 2003, 2004; Visscher & Fegley 2006), it is unclear how important photochemistry will be in determining the abundances of these species at pressures of tens to hundreds of millibar. CS06 did explore other effects such as

TABLE 1
Chemistry Cases

Case	X_{CH_4}	X_{CO}	X_{H_2O}	CH_4/CO Ratio
0.................	Equilibrium	Equilibrium	Equilibrium	Equilibrium
1.................	6.60E-6	4.81E-4	2.75E-4	0.014
2.................	1.50E-8	4.88E-4	2.69E-4	3.0E-5

Note.—Mixing ratios are given for each chemistry case. Abundances from equilibrium chemistry calculations are used when specified.

Fig. 4.—Mixing ratios of CH_4, CO, and H_2O, as function of pressure, along three P-T profiles in the atmosphere of HD 209458b. These profiles are the one-dimensional profile from Fortney et al. (2005) in gray, the subsolar point of the CS06 simulation, in thin black, and the antistellar point of the CS06 simulation, in thick black. Arrows at the top of the plot indicate the fixed mixing ratios of cases 1 and 2 chemistry, given in Table 1.

atmospheric metallicity and temperature. If the atmosphere is greater than $[M/H] = 0.0$, or if the atmosphere is hotter, the CH_4/CO ratio would be even smaller. See CS06 for additional discussion.

In our spectral calculations, we find that significant differences arise depending on our treatment of chemistry. We will therefore investigate the effects of a few chemistry cases, as explained below, and shown in Table 1. We label our equilibrium chemistry trial "case 0," as it is the standard case. For "case 1," we fix the CH_4/CO ratio at 0.014 (as found by CS06) at all temperatures and pressures along the profiles. Consistently incorporating the increasing CH_4/CO ratio at depth ($P > 1$ bar) would be difficult with previously tabulated opacities, and would have little to no effect on the emergent spectra. Recall that 23% of available oxygen is lost to the formation of Mg-silicate clouds (Lodders 2003), which in this model have cloud bases near 1 kbar. The remaining oxygen is almost entirely found in CO and H_2O. As the CH_4 and CO abundances are fixed, for case 1 we will also fix the abundance of H_2O; the mixing ratios of CH_4, CO, and H_2O are consistent with the amount of available oxygen at $T \sim 1200$ K and pressures of tens of millibars. We also briefly consider a "case 2," in which the CH_4/CO ratio has been further reduced, in an ad hoc manner, which could be due to quenching of the abundances at a hotter temperature or the photochemical destruction of CH_4. The CH_4/CO ratio is reduced by nearly a factor of 500, to 3×10^{-5}. The mixing ratios of CO and H_2O are nearly the same as in case 1, although the slightly increased CO abundance (due to the drop in the abundance of CH_4 and conservation of carbon atoms) uses up some oxygen at the expense of H_2O. This case is valuable for comparison purposes because it shows the spectral effects of a negligible CH_4 abundance. In all cases, the mixing ratios of all other chemical species are given by equilibrium values. However, only CH_4, CO, and H_2O have a discernible impact on the spectra.

In Figure 4 we plot mixing ratios of CH_4, CO, and H_2O predicted from equilibrium chemistry along three P-T profiles in the atmosphere of HD 209458b. In gray are the mixing ratios for the one-dimensional profile of Fortney et al. (2005). The abundance of CH_4 is negligible. In thin black and thick black are the mixing ratios at the substellar point and the antistellar point, respectively, of the CS06 simulation. The dominant carbon carrier is clearly CO, rather than CH_4, except at $P < 100$ mbar for the antistellar point. Most of the night side has a chemistry profile similar to the antistellar point, and hence, strong CH_4 absorption will be seen. At the top of the plot, arrows indicate the assigned mixing ratios of cases 1 and 2 for these three molecules.

In § 3 we make quantitative comparisons to current ground-based and space-based infrared data. While we find that the agreement is good for the model presented here, we wish to stress that this study is exploratory. This is the first study that quantitatively explores the influence of atmospheric dynamics on the emergent spectra of a hot Jupiter atmosphere. The greatest uncertainty likely lies in the calculation of heating/cooling rates with a simple Newtonian cooling scheme in the dynamical model, as discussed
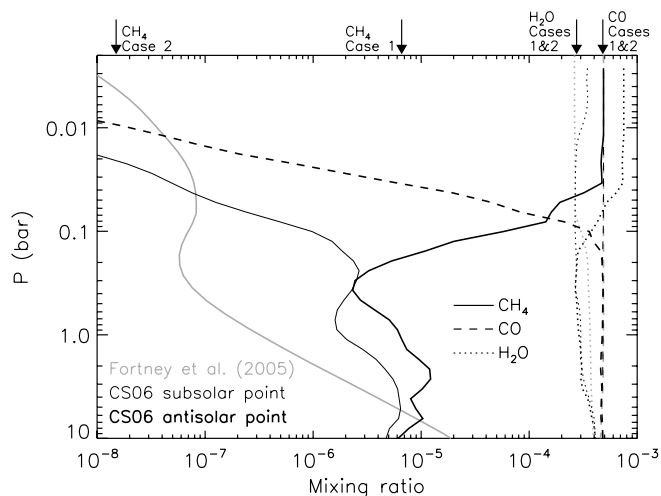
in Cooper & Showman (2005) and CS06. Another issue is that CS06 calculate temperature deviations from a one-dimensional radiative-convective profile published in Iro et al. (2005). However, our emergent spectrum is calculated using our radiative transfer solver, which is a different code, and we use different abundances (Lodders 2003) than these authors (Anders & Grevesse 1989). However, we find that when solving the radiative transfer for the Iro et al. profile we obtain a T_{eff} that differs by only 1% from their value.

In their nonequilibrium chemistry work, CS06 chose the abundances of Lodders & Fegley (1998), while here we use (Lodders 2003), in order for the most natural comparison with our previous work (Fortney et al. 2005, 2006). Obviously no choice would be fully self consistent. However, the choice of elemental abundances is certainly a smaller concern than the current debate concerning the correct chemical timescale for conversion of CO to CH_4 in planetary atmospheres (see Yung et al. 1988; Fegley & Lodders 1994; Griffith & Yelle 1999; Bézard et al. 2002; Visscher & Fegley 2005). In addition, CS06 have shown that a 300 K decrease in temperature, for instance, leads to a twentyfold increase in CH_4/CO (see § 5.3), so temperature uncertainties likely swamp any abundance issues. We stress that our focus in the following sections is on highlighting the spectral differences between a model that accounts for dynamical redistribution of energy around the planet and one that does not. Indeed the magnitude of the spectral effect suggests that additional, more internally self consistent work, is clearly appropriate.

3. INFRARED SPECTRA

3.1. Spectra as a Function of Orbital Phase

We now turn to the predicted infrared spectrum of our dynamical model atmosphere. As has been shown by many authors since Seager & Sasselov (1998) the infrared spectra of hot Jupiters are believed to be carved predominantly by absorption by H_2O, CO, and, if temperatures are cool enough, CH_4. In general, absorption features of hot Jupiters are predicted to be shallower than brown dwarfs of similar effective temperature and abundances. This is predicated on hot Jupiters having a significantly shallower
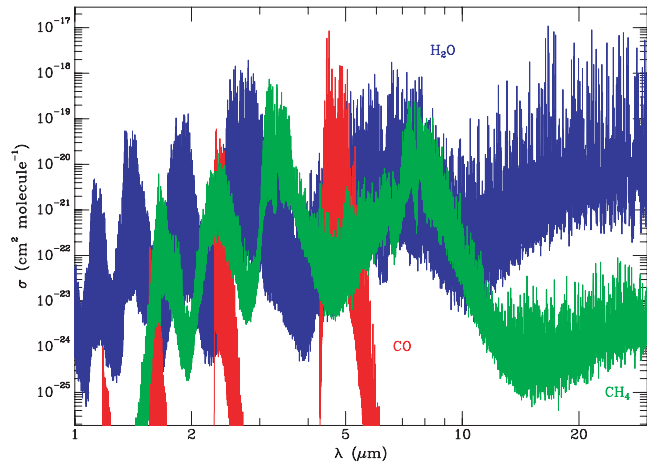
Fig. 5.—Absorption cross sections vs. wavelength for H_2O (*blue*), CO (*red*), and CH_4 (*green*) at 1200 K and 100 mbar. These cross sections are not weighted by abundance.

Fig. 6.—Planetary emergent flux density (ergs s^{-1} cm^{-2} Hz^{-1}) vs. wavelength as a function of orbital phase for case 0 equilibrium chemistry. The spectra are color-coded with the diagram in the upper right corner of the figure. All spectra are calculated at intervals of $60°$. The black spectrum is for the night side of the planet, which is seen during transit. The red spectrum is $60°$ later. The dark blue spectrum shows the planet during secondary eclipse ($180°$), when the fully illuminated hemisphere is visible. The magenta spectrum is $300°$ after transit. The dashed black curve is the flux of a 1330 K blackbody, which plots behind the dark blue curve at $\lambda > 4$ μm. Normalized *Spitzer* band passes are shown in dotted lines at the bottom and standard H, K, L, and M bands are shown at the top.

atmospheric temperature gradient, which is due to the intense external irradiation by the parent star. Figure 5 shows absorption cross sections per molecule for CH_4, CO, and H_2O from 1 to 30 μm. To avoid clutter on our spectral plots, we will not label absorption features, so referring to Figure 5 will be helpful.

Our first spectral calculation is for case 0 chemistry, as a function of orbital phase. This is shown in Figure 6. We show the emitted spectrum at six orbital locations: zero (during the transit), 60, 120, 180 (during the secondary eclipse), 240, and 300 degrees, where the degrees are orbital degrees after transit. At $0°$ (*black spectrum*), we see the full night side of the planet. The temperature gradient is fairly steep, leading to deep absorption features. Most carbon is in the form of CH_4, leading to strong methane absorption in bands centered on 1.6, 2.2, 3.3, and 7.8 μm. Absorption due to H_2O at many wavelengths is also strong. Absorption due to CO at 2.3 and 4.5 μm is quite weak, due to its small mixing ratio.

Sixty degrees later (*red spectrum*), the hemisphere we see is $\frac{2}{3}$ night and $\frac{1}{3}$ day. The part of the day hemisphere we see has the hot west-to-east jet coming toward us. This will later be an interesting point of comparison with the $300°$ spectrum (*magenta*), which is also $\frac{2}{3}$ night. Here all absorption features are muted because, due to the jet shown in Figure 1, more than $\sim\frac{1}{3}$ of the planet is showing the nearly isothermal profiles representative of the day side. These profiles lead to a blackbody-like spectrum. At $120°$ (*in green*), we are seeing $\frac{2}{3}$ day side, and that part of the day side is the hottest, due to the wind from the west blowing the hot spot downstream. The absorption features have become very weak.

The peak in total infrared flux actually occurs $153°$ after transit. During the secondary eclipse, $27°$ later, the planet is less luminous. During the secondary eclipse (*in dark blue*) the planetary spectrum is essentially featureless longward of 1.8 μm. The fully illuminated hemisphere possesses profiles that are nearly isothermal in our pressure range of interest. Intriguingly, this leads to a spectrum that is very similar to a blackbody. For comparison, we plot a dashed black curve that is the thermal emission of a 1330 K blackbody. It plots behind the $180°$ spectrum for all $\lambda > 4$ μm.

As we move to orbital phases after the secondary eclipse, we see that the spectra are not symmetric with their reflections on the other half of the orbit. The light blue spectrum is significantly lower than the green one, even though at both points we are seeing
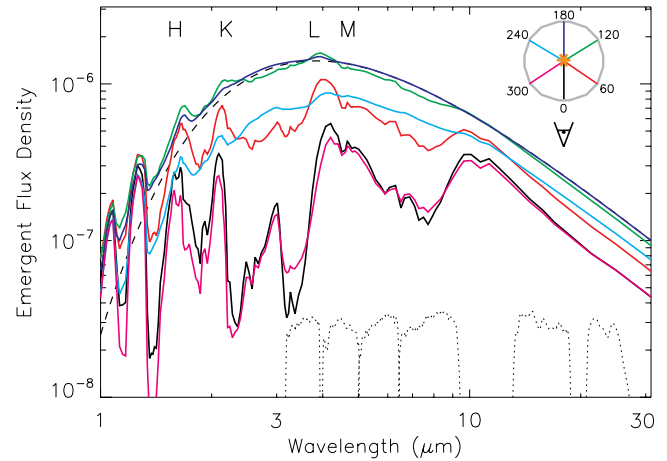
$\frac{2}{3}$ day and $\frac{1}{3}$ night. This is again due to the west-to-east jet. At $240°$, the hottest part of the day side is not in view. At $300°$ (*in magenta*) $\frac{1}{3}$ of our view is the coolest part of the day side, along with $\frac{2}{3}$ of the night side. The spectrum is quite similar to what was seen during the transit. The planet appears least luminous $31°$ before transit.

3.2. *Spectra with Alternate Chemistry*

Since CS06 find significant deviations from equilibrium carbon chemistry, it is useful to examine spectra with nonequilibrium chemistry. We now investigate the spectra using cases 1 and 2. Figure 7 shows comparison spectra at two orbital phases: zero and $180°$, which is during transit and secondary eclipse, respectively. On the day side, we see that the emergent spectrum is essentially exactly the same, independent of chemistry. Because the P-T profiles are nearly isothermal, essentially no information about the chemistry can be gleaned from the spectrum. For comparison with our previous work, in Figure 7 we plot with a dotted line the cloudless planetwide average spectrum of HD 209458b from Fortney et al. (2005), which shows absorption due to H_2O and CO and strong flux peaks between these absorption features.

We will now examine the small inset in Figure 7. This is a zoom-in of the secondary-eclipse spectra near 2.2 μm. The three thick horizontal bars connected by dashes make up an interesting observational 1 σ upper limit that was first reported in Richardson et al. (2003a). These data were analyzed again and presented in Seager et al. (2005). The measurement was a relative one; only the vertical distance between the central band and two side bands is important: they can be moved up or down as a group. Specifically, the flux in the central band cannot exceed the combined flux in the two adjacent bands by an amount greater than vertical distance shown (which is 0.45×10^{-6} ergs s^{-1} cm^{-2} Hz^{-1}). Our dynamical dayside spectra, which are nearly featureless due to the nearly isothermal atmosphere, easily meet this constraint. We note that an upper limit obtained by Snellen (2005) in K band,
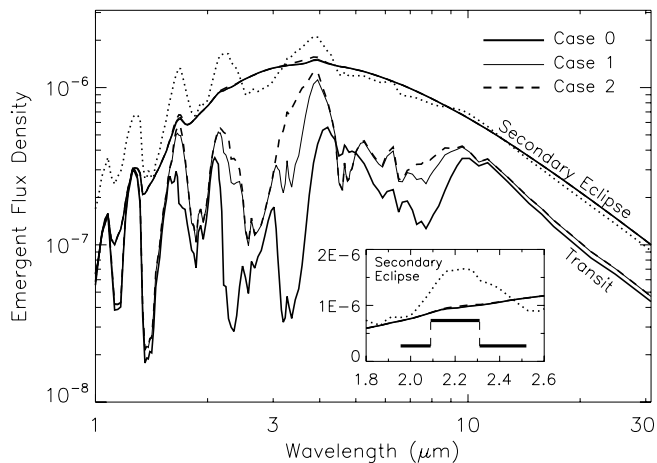
Fig. 7.—Planetary emergent flux density (ergs s^{-1} cm^{-2} Hz^{-1}) vs. wavelength at two orbital phases for all three of our chemistry cases. The spectrum at 180°, during the secondary eclipse, is essentially the same for all three cases. At 0°, during the transit, CH$_4$ is very abundant in the case 0 trial, leading to deep absorption features centered at 1.6, 2.2, 3.3, and 7.8 μm. Absorption due to CO is muted in case 0, but is strong in cases 1 and 2. Water vapor absorption is strong in all cases. *Inset*: Zoom near 2.2 μm. The three thick horizontal lines connected by dashes are a constraint on the maximum relative height of the flux peak at 2.2 μm (middle band), compared to the average of the flux in the two adjacent bands, from Seager et al. (2005). The bars can be shifted together vertically. (See text.)

which covers a similar wavelength range, has an error bar that is too large to distinguish among published models.

In contrast to the models presented here that include dynamics, published one-dimensional models to date all predict large flux differences between 2.2 μm and the surrounding spectral regions when abundances are solar. The one-dimensional models with solar abundances presented in Seager et al. (2005), for example, were not able to meet the 2.2 μm flux-difference constraint, because the H$_2$O bands adjoining the 2.2 μm flux peak were too deep. Seager et al. (2005) suggested that if C/O > 1, then little H$_2$O would exist in the atmosphere, and the observational constraint could be met. Here, we propose instead that dynamics produce a relatively isothermal dayside temperature, in which case the constraint can easily be met even with solar C/O.

Nevertheless, the observational constraint is not yet firm enough to fully rule out the one-dimensional radiative-equilibrium models at solar abundances. The Fortney et al. (2005) solar-abundance models, for example, marginally meet the current observational flux-difference constraint. (Fortney et al. 2005 find a flux difference of 0.43 × 10^{-6} ergs s^{-1} cm^{-2} Hz^{-1}.) The cause for the discrepancy between the one-dimensional models in Fortney et al. (2005) and Seager et al. (2005) remains unclear but could occur if the *P-T* profiles in Seager et al. were steeper than those in Fortney et al., leading to deeper bands in the former study. More precise flux-difference observations like that of Richardson et al. (2003a) during secondary eclipse would help confirm or rule out the one-dimensional solar-abundance models. Even a factor of 2 decrease in the observational upper limit between the "in" and "out" bands could rule out the solar-abundance Fortney et al. (2005) model, while supporting the isothermal-dayside models (e.g., CS06) and the C/O > 1 models with weak water bands. Alternatively, the detection of a small flux peak at 2.2 μm would lend support to the one-dimensional models with C/O < 1, while constraining the temperature gradient on the planet's dayside.

The fact that both the solar-abundance CS06 models (presented here) and the radiative-equilibrium one-dimensional models with C/O > 1 produce almost no flux difference between 2.2 μm and

the surrounding continuum implies that the 2.2 μm band cannot be used to distinguish between these alternatives. Instead, additional constraints at other wavelengths will be necessary to discriminate between them. Measurements of flux differences surrounding CO (rather than H$_2$O) bands could provide such a test. The radiative-equilibrium C/O > 1 models, although lacking water bands, would presumably have strong CO bands and would hence predict a strong flux difference between the center of a CO band and the surrounding continuum. On the other hand, because the dayside atmosphere is nearly isothermal in the CS06 models, these circulation-altered models would predict little flux difference between the CO band and the surrounding regions even in the presence of large quantities of CO. An observation of minimal flux difference across CO bands as well as H$_2$O bands would support isothermal-dayside models like CS06 while arguing against the radiative-equilibrium one-dimensional models with steep temperature gradients.

Although observations of TrES-1 may not be directly applicable to HD 209458b, as TrES-1 may have a T_{eff} 300 K cooler, there is an important issue to note for our discussion here. The models of Fortney et al. (2005), Seager et al. (2005), and Barman et al. (2005) show a mid-infrared spectral slope that is bluer than observed from 4.5 to 8.0 μm by Charbonneau et al. (2005) for TrES-1, although the model of Burrows et al. (2005) appears to be consistent with this slope. Showman & Cooper (2006) and Fortney et al. (2006) have discussed that models with an atmospheric temperature inversion would give infrared spectra with a redder spectral slope, due to molecular emission features, in better agreement with observations. The CS06 model of the day side of HD 209458b, which lacks the strong negative temperature gradient of these radiative equilibrium models, also leads to a redder mid-infrared spectral slope.

On the planet's night side, we see significant spectral differences between the three chemistry cases. In cases 1 and 2, the CH$_4$ mixing ratio is constrained to a small abundance, weakening these absorption features. Absorption due to CH$_4$, CO, and H$_2$O is readily seen in case 1. Case 2 shows essentially the same CO and H$_2$O absorption, but CH$_4$ absorption is no longer seen. The transition, as a function of orbital phase from deep to essentially nonexistent absorption features in cases 1 and 2, are similar to what was seen in case 0. In the interest of conciseness, and because case 2 is ad hoc, hereafter we concentrate on cases 0 and 1. The spectra for cases 1 and 2 are essentially the same, except in regions of CH$_4$ absorption; we will highlight these differences when necessary. It is important to remember that in case 1 and case 2 chemistry, the mixing ratios of our principal absorbers, CH$_4$, CO, and H$_2$O are fixed. Therefore, changes in the spectra with orbital phase are only due to changes in the planetary *P-T* profiles on the visible disk, due to the rotation of the planet through its orbit.

One can integrate the spectrum of the planet's visible hemisphere over all wavelengths, as a function of orbital phase, to determine the apparent luminosity of the planet at all phases. Here we divide out $4\pi R^2\sigma$ to calculate the apparent effective temperature (T_{eff}) of the visible hemisphere. This is plotted in Figure 8 for cases 0 and 1. We can clearly see that in both cases, the time of maximum flux precedes the time of secondary eclipse by ~27°, or 6.3 hr. Since the spectra of the two cases overlap around the time of secondary eclipse, so do the plots of T_{eff}. At other orbital phases, the case 0 curve always plots lower. The largest effect is before the time of transit. The effect is tied to the CH$_4$ abundance. If CH$_4$ is able to attain a large mixing ratio, it leads to an atmosphere that has a higher opacity, meaning one cannot see as deeply into the atmosphere. One then reaches an optical depth of ~1 higher in the atmosphere, which is significantly cooler for nightside *P-T*
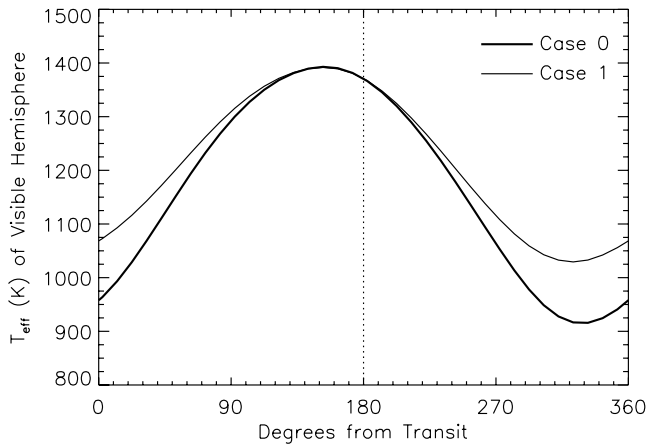
FIG. 8.—Effective temperature of the visible hemisphere of HD 209458b as a function of orbital phase for two chemistry cases.

profiles, leading to a lower T_{eff}. The point of minimum planetary flux precedes the transit by $31°-37°$, depending on the chemistry.

In their (very similar) previous dynamical model, Cooper & Showman (2005) predicted a time of maximum planetary flux of $60°$ (or 14 hr) before secondary eclipse. The large timing difference between that work and this one is due almost entirely to the choice of "photospheric pressure" made in Cooper & Showman (2005). They chose a pressure of 220 mbar in their work, which is deeper than the "mean" photosphere that we find here. At higher pressure, the radiative timescales are longer, such that winds are able to blow the atmosphere's hottest point farther downstream. Cooper & Showman (2005) and CS06 previously discussed how their prediction varied as a function of the chosen photospheric pressure.

4. INFRARED LIGHT CURVES

4.1. Spitzer Bands

For the foreseeable future, the most precise data for understanding the atmospheres of hot Jupiters will come from the *Spitzer Space Telescope*. For HD 209458b, only an observation at 24 μm (the shortest wavelength MIPS band), has been published. It seems likely that observations in all four IRAC bands (3.6, 4.5, 5.8, and 8.0 μm), as well as IRS at 16 μm, will be obtained within the next year or two. As such, we have integrated the spectra of our planet models and a Kurucz (1993) model of star HD 209458 over the *Spitzer* bands in order to generate planet-to-star flux ratios as a function of orbital phase. These are plotted for cases 0 and 1 in Figure 9. The stellar model fits the stellar parameters derived in Brown et al. (2001) and is the same model used in Fortney et al. (2005).

The behavior of the planet-to-star flux ratios is quite interesting. While the T_{eff} of the planet was found to reach a maximum $27°$ before secondary eclipse, the behavior in individual bands is more varied. For instance, in both chemistry cases, the planetary flux in the 24 μm band peaks only $15°$ before secondary eclipse. This is because the "photospheric pressure" is at a lower pressure in this band than the planet's "mean photospheric pressure." As previously discussed, at lower pressures, the radiative time constants are shorter, and the atmosphere is able to more quickly adjust to changes in incident flux. At higher pressure, winds are better able to blow the planet's hot spot downstream. One should keep in mind that the light curves generated are a function of the dynamical calculation and the radiative transfer. It is the radiative transfer calculation that determines how deeply into the atmosphere (and therefore, to what temperature) we see.
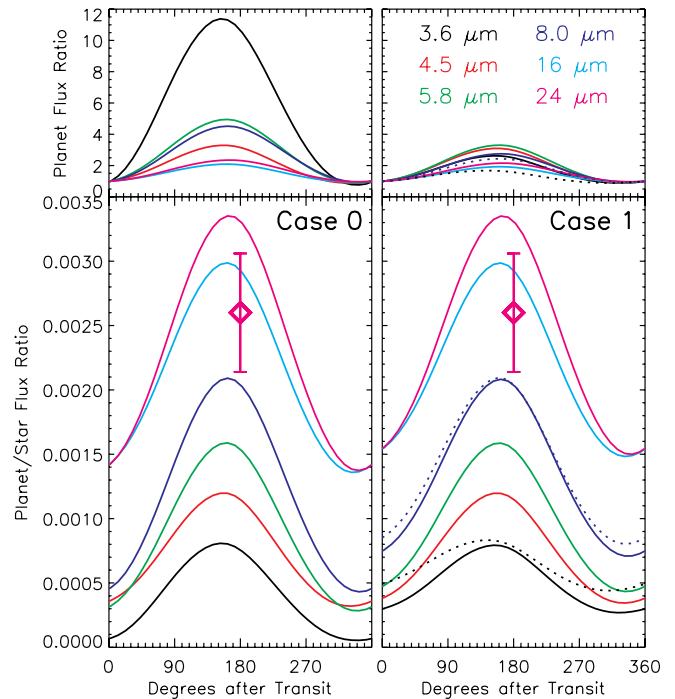

FIG. 9.—Planetary flux in *Spitzer* bands as a function of planetary orbital phase. The left panels are case 0 and right panels case 1. The bottom panels show the HD 209458b planet-to-star flux ratios. The top panels show the planetary flux at every phase divided by the planetary flux seen during the transit (at $0°$). The dotted lines indicate predictions for case 2 chemistry. At $180°$ is the Deming et al. (2005) secondary eclipse observation at 24 μm, with 1 σ error bars (0.00260 ± 0.00046). This is shown in magenta, which is the color used for the 24 μm curve.

The 3.6 μm band peaks earliest, $\sim27°$ before transit, as the T_{eff} does as well. This band shows a fifteenfold variation in flux (peak to trough) as a function of orbital phase for case 0 because it encompasses a significant CH_4 absorption feature that waxes and wanes. Since the abundances of CH_4 and CO are not free to vary in case 1, the flux ratios in this case do not show the large amplitudes found in some bands in case 0. The dotted lines in the case 1 panels are for case 2 in the 3.6 and 8.0 μm bands, where CH_4 absorption occurs. The flux variation in these bands is even further reduced as CH_4 absorption is not seen (see Fig. 7.) At 24 μm, our model is 1.6 σ higher than the secondary eclipse data point published by Deming et al. (2005) indicating that the planet may be dimmer at $180°$ than we predict. In all bands, differences in chemistry between the two cases have essentially no effect on the timing of the maxima in planetary flux. However, since the night side is much more sensitive to chemistry, the minima can vary by as much as $20°$ in bands that are sensitive to CH_4 absorption.

4.2. Standard Infrared Bands

The results of ground-based observations of flux from hot Jupiters have been mixed. All searches for visible light have yielded only upper limits (Charbonneau et al. 1999; Collier Cameron et al. 2002; Leigh et al. 2003), which have ruled out some models with bright reflecting clouds. In the near infrared, specifically for HD 209458b, Richardson et al. (2003a, 2003b) have constrained molecular bands of CH_4 and H_2O. The constraint on emission at 2.3 μm between H_2O absorption features was shown in Figure 7. The predicted planet-to-star flux ratio really does not become favorable until wavelengths longer than 3 μm, which may continue to challenge observers.
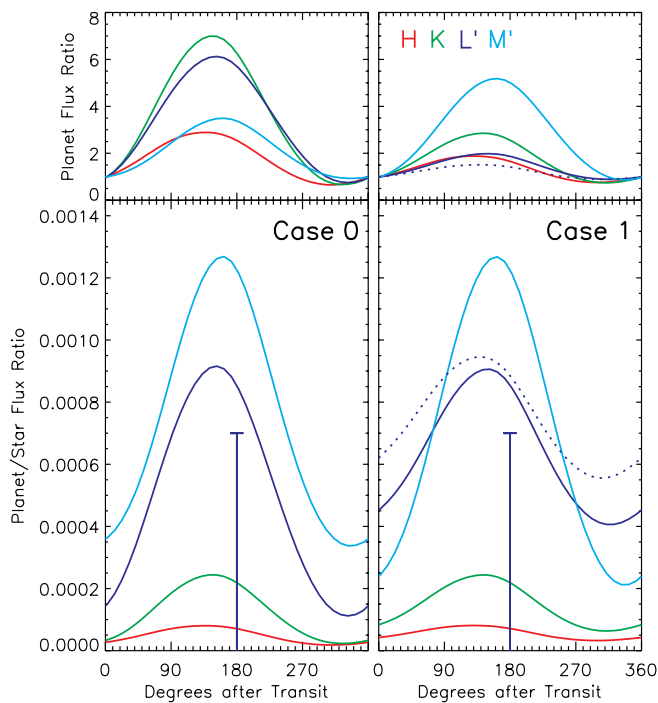
Fig. 10.—Planetary flux in MKO infrared bands as a function of planetary orbital phase. The left panels are case 0 and right panels case 1. The bottom panels show the HD 209458b planet-to-star flux ratios. The top panels show the planetary flux at every phase divided by the planetary flux seen during the transit (at 0°). The dotted line indicates a prediction for case 2 chemistry. At 180° is the Deming et al. (2006b) secondary eclipse observation at L' band, with 1 σ error bars. The observation is -0.0007 ± 0.0014, so the actual data point is well off of the bottom of the plot. This is shown in dark blue, which is the color used for the L' curve.

In Figure 10 we plot planet-to-star flux ratios in the Mauna Kea Observatory (MKO) H ($\sim$1.6 μm), K ($\sim$2.2 μm), L' ($\sim$3.8 μm), and M' ($\sim$4.7 μm) bands. Since the wavelength ranges of the L' and M' bands have significant overlap with the IRAC 3.6 and 4.5 μm bands, the predicted ratios are quite similar. In dark blue, we show the L'-band upper limit of -0.0007 ± 0.0014 from Deming et al. (2006b). The model is just above the 1 σ error bar.[5] This is a better match than is attained with one-dimensional radiative equilibrium models (Deming et al. 2006b), which predict a flux peak just short of 4 μm, as shown in Figure 7. The Fortney et al. (2005) HD 209458b radiative equilibrium model, which has somewhat muted flux peaks compared with similar models by other authors, has a planet-to-star flux ratio of 0.00114 in L' band. In dotted blue in the case 1 panels is our L' band (which encompasses CH_4 absorption) prediction for case 2 chemistry. Looking at shorter wavelengths, in the H and K bands, the planet is predicted to be dimmer, while the star is brighter, leading to low flux ratios. The peak emission in these bands does occur earlier than in the *Spitzer* bands. For instance, the H-band peak is 42° before secondary eclipse.

5. DISCUSSION

5.1. *Effective Temperature*

For the CS06 dynamical model of the atmosphere of HD 209458b, we find that the apparent $T_{\rm eff}$ of the visible hemisphere

---

[5] As described in Deming et al. (2006b) this observation was actually performed in a narrow band centered on 3.8 μm, within the standard L' band. Our calculated planet-to-star flux ratio at secondary eclipse increases by 4% when using this narrow band, compared to standard L'. Since this is a small correction, our conclusions are unchanged.

is strongly variable, with a maximum of 1390 K and a minimum of 915 K for equilibrium chemistry and 1025 K for (the probably more realistic case of) disequilibrium chemistry. This leads to a luminosity of the visible planetary hemisphere that varies by factors of 5.3 and 3.4, respectively for these two cases. For the one-dimensional Iro et al. (2005) planetwide profile, we derive a $T_{\rm eff} = 1325$ K, 1% less than found by the authors. The dayside $T_{\rm eff}$ for the dynamical model is not significantly larger than this planetwide $T_{\rm eff}$. As an additional comparison, we calculate the mean of the planetary luminosity over the entire orbit and then convert to $T_{\rm eff}$ to find a mean $T_{\rm eff}$ for cases 0 and 1. This gives $T_{\rm eff}$ values of 1195 and 1227 K, respectively, showing that the CS06 model, at the pressures levels that radiate to space, is as a whole somewhat colder than the one-dimensional profile of Iro et al. (2005). This is likely a consequence of the radiative forcing scheme employed in CS06, which will be reinvestigated when models that consistently couple radiative transfer and dynamics are developed.

The $\sim$400 K $T_{\rm eff}$ contrasts found are predominantly due to changes in the temperature structure of the hemisphere that is visible as function of orbital phase. In addition, atmospheric opacity makes an important contribution when the CH_4/CO ratio is free to vary with pressure and temperature. When the CH_4 mixing ratio is below that predicted by equilibrium chemistry, this leads to a lower opacity atmosphere, for a given P-T profile. While the few individual bands of CO are somewhat stronger than those of CH_4, CH_4 absorption across the planet's broad the 2–10 μm flux peak dominates over the two bands of CO. One is able to see more deeply into a CH_4-depleted atmosphere, leading to a higher $T_{\rm eff}$.

5.2. *HD 209458b Infrared Data*

Currently, the only published secondary eclipse datum from *Spitzer* for HD 209458b is the 24 μm detection of Deming et al. (2005). The models presented here have a planet-to-star flux ratio during secondary eclipse that is 1.6 σ larger than this observational data point. Together with our excellent agreement with the ground-based data at 2.3 μm from Richardson et al. (2003a) and Seager et al. (2005) and our 1.1 σ difference with the 3.8 μm data from Deming et al. (2006b), we regard this as excellent agreement— significantly better than has been previously obtained with one-dimensional radiative equilibrium models.

It is interesting to discuss a few issues that arise if the flux ratios are indeed 10%–25% less than we calculate here, as indicated by the L' and 24 μm band data. For instance, perhaps day-night temperature contrasts in the atmosphere are not as large as predicted by CS06, leading to smaller deviations from a "planetwide" $T_{\rm eff} \sim 1200$ K. This may involve radiative time constants that are significantly longer than predicted by Iro et al. (2005), winds faster than predicted by CS06, or both. It would be worthwhile for other groups that possess hot Jupiter radiative transfer codes to compute radiative time constants at these temperatures and pressures. This is an area that we will pursue in the near future.

Another possibility for a smaller planet-to-star flux ratio during secondary eclipse would be if the planet had a larger Bond albedo than calculations currently indicate. This would mean less absorbed stellar flux and correspondingly lower temperatures everywhere on the planet. Cooler temperatures everywhere on the planet would lead to chemical abundances that differ from our previous cases. More CH_4 would form, at the expense of CO, which would also lead to a slightly higher mixing ratio for H_2O, which shares oxygen with CO.

Hot Jupiters are believed to have very low Bond albedos—on the order of 90% or more of incident stellar flux is expected to be absorbed. In Fortney et al. (2005) we found that our one-dimensional
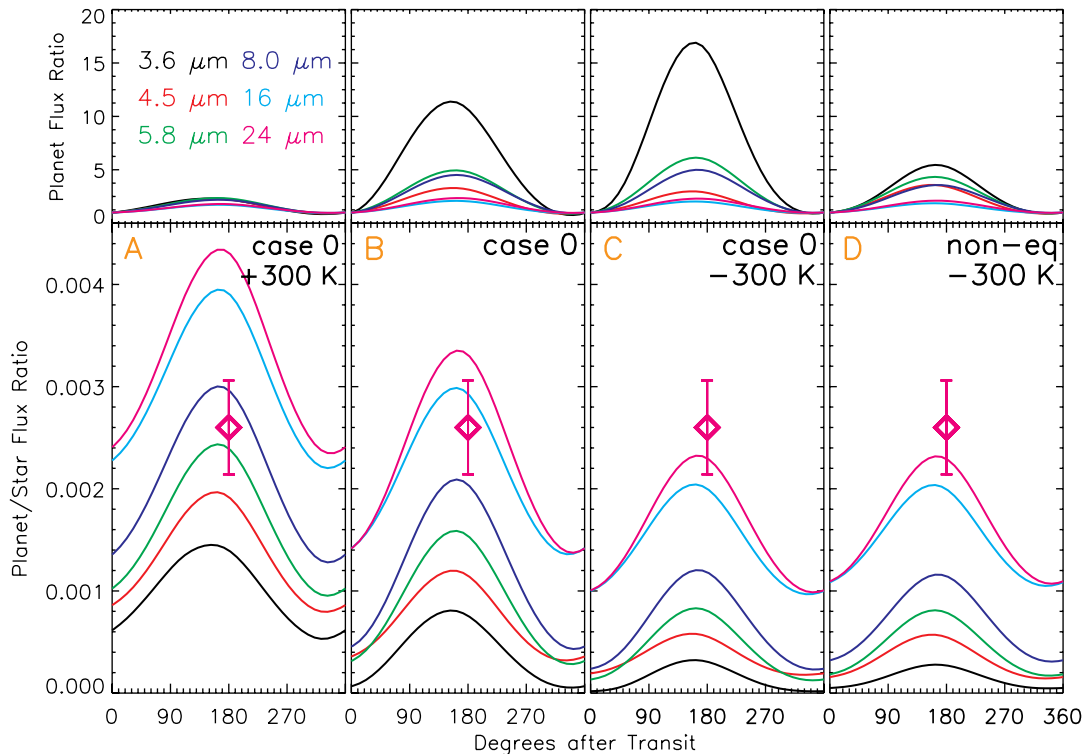
Fig. 11.—Planetary flux in *Spitzer* bands as a function of planetary orbital phase. The light curves in panels *a*, *b*, and *c* assume equilibrium chemistry, while panel *d* uses nonequilibrium chemistry. The bottom panels show the HD 209458b planet-to-star flux ratios. The top panels show the planetary flux at every phase divided by the planetary flux seen during the transit (at 0°). Panel *a* shows the CS06 simulation with a 300 K increase in temperature. Panel *b* shows the nominal case 0 simulation, previously shown in Fig. 9*a*. Panel *c* shows the CS06 dynamical simulation with a 300 K temperature decrease. Panel *d* is also the simulation with the 300 K temperature decrease, but uses nonequilibrium chemistry with a fixed CH₄/CO ratio of 0.20. (See text.) For all panels, the Deming et al. (2005) datum at 24 μm is shown.

model atmosphere for HD 209458b scattered only 8% of incident flux. For TrES-1, this was 6%. To date, there is at least a hint that the Bond albedo of TrES-1 may have been underestimated. Charbonneau et al. (2005) under the assumption that the planet emits as a blackbody, determined a Bond albedo of 0.31 ± 0.14 from their *Spitzer* IRAC observations at 4.5 and 8.0 μm. Perhaps hot Jupiters are not quite as hot as had been previously thought. However, this determination should be considered very preliminary at this time.

Richardson et al. (2006) have recently observed the *transit* of HD 209458b at 24 μm, as well. From an observed transit depth of 0.0149 ± 0.0003, they determined the radius of the planet in this band to be $(1.26 \pm 0.08)R_J$, which includes uncertainties in the stellar radius. Our model predicts a change in the apparent planet-to-star flux ratio of ~ 0.00008 during the 20° of the Richardson et al. (2006) transit observations, ~ 4 times smaller than their uncertainty, and hence too small to have been detected. As was seen in Figures 9 and 10, the change in planetary flux as a function of orbital phase is not as pronounced near the time of transit (and secondary eclipse) as it is at other phases.

5.3. *Temperature Sensitivity*

To illustrate the sensitivity of our results to temperature changes, we have computed spectra as a function of orbital phase, using equilibrium (case 0) chemistry for two additional models. These are additional dynamical models described in CS06, in which the base *P-T* profile of Iro et al. (2005) has been increased or decreased by 300 K, with correspondingly warmer or colder night sides. The full dynamical simulations have been run again with these parameters. The resulting light curves, in *Spitzer* bands, are shown in Figures 11*a*, and 11*c*. For the "cold" (-300 K) model

CH₄ is the dominant carbon carrier on the night hemisphere, and CO on the day hemisphere, leading to large flux variation in excess of that found for our nominal CS06 simulation, as shown in Figure 11. For the "hot" ($+300$ K) model, on both the day and night hemispheres, CO is the dominant carbon carrier. Methane absorption features are very weak on the night side, leading to flux variations in every band no larger than a factor of 2.7 from peak to trough. This model is somewhat similar to our earlier case 2, but at warmer temperatures, as at all phases CO is the dominant carbon carrier. Fluxes are everywhere greater in the hot model than the nominal model, and everywhere less in the cold model than in the nominal model. This is due to the differing atmospheric temperatures. The cold model best fits the Deming et al. (2005) datum at 24 μm. In addition, the phase of maximum and minimum flux in a given band can change by up to $\sim 10°$ between these simulations, due both to differing chemistry and atmospheric dynamics. As discussed in Cooper & Showman (2005) and CS06, while these models all possess similarly strong east-to-west jets, the dynamical atmospheres differ slightly in detail.

CS06 also examined nonequilibrium CH₄/CO chemistry for these models. For the "cold" (-300 K) model, nonequilibrium chemistry was important, and the CH₄/CO ratio at $P < 1$ bar became homogenized at 0.20 around the entire planet. This ratio was 0.014 for the nominal case 1 described earlier. For the cold model, equilibrium chemistry would predict a night side dominated by CH₄ and a day side dominated by CO. For the "hot" model ($+300$ K) both equilibrium and nonequilibrium chemistry predicts that CO is the dominant carbon carrier on both the day and side hemispheres. Figure 11*d* shows our computed flux ratios for nonequilibrium chemistry for the cold case. As was

shown previously for our nominal case, flux variation is smaller with nonequilibrium chemistry, because the mixing ratios of CH_4, CO, and H_2O are the same on the night and day hemispheres. Again, because of the nearly isothermal temperature structure of the day side, chemical abundances have little effect on the day-side planet-to-star flux ratios, which are nearly equal for these two chemistry cases.

These additional cases further highlight the importance of CH_4/CO chemistry in the computation of infrared light curves. Infrared fluxes as a function of orbital phase are sensitive to the temperatures of the hemisphere facing the observer, as well as the abundances of important molecular absorbers. For planetary P-T profiles that cross important CH_4/CO chemical boundaries, as most hot Jupiters surely do, whether or not these species are found in their equilibrium mixing ratios has a major impact on resulting infrared flux in *Spitzer* bands, especially on the night side.

5.4. *The Future and Conclusions*

From the size of the error bar from the Deming et al. (2005) 24 μm observations, it is clear that, could this instrument stability be sustained over the course of tens of hours of observations, the change in flux over time presented here could be detected. One-half of an orbital period for HD 209458b is 42 hr. If flux in the 8.0 μm band for HD 209458b is higher than models predict, as was the case for TrES-1 (Fortney et al. 2005; Barman et al. 2005), then this would be an attractive band as well, as the error bars should be smaller.

What might one hope to see with sustained observations? If the peak in infrared flux does occur only $\sim 25°$–$30°$ before secondary eclipse, this would be difficulty to discern. However, the detection of any sort of ramp up in flux from the time of transit to secondary eclipse would give us important information on the day-night temperature contrast. The recently discovered transiting planet HD 189733b (Bouchy et al. 2005) would likely be an even more attractive target, as the planet-star flux ratios are likely twice as large (Fortney et al. 2006; Deming et al. 2006a), and the orbital period is $\sim$40% shorter. We predict secondary eclipse planet-to-star flux ratios for this system in Fortney et al. (2006); our calculation at 16 μm is a good match to the published observation of Deming et al. (2006a).

A clear prediction from our calculations here is that when one uses realistic nonequilibrium chemistry calculations, the change in planetary flux as a function of orbital phase is greatly reduced, relative to equilibrium chemistry calculations, because the atmosphere's composition is fixed. For the *Spitzer* bands, for case 0, the maximum flux variation is in the 3.6 μm band, which varies by a factor of 15 from peak to trough. The minimum variation is a factor of 2.2, in the 16 μm band. For case 1, this variation drops significantly, and the maximum variation is a factor of 3.7, in the 5.8 μm band, and the minimum is 2.0, again in the 16 μm band. We suggest that the 5.8 and 8.0 μm bands may be the best *Spitzer* bands in which to search for flux variations as a function of orbital phase, as these bands combine a high planet-to-star flux ratio and the sensitivity and stability of the IRAC detectors.

If the dayside thermal emission of hot Jupiters is similar to a blackbody, as we find here, problems arise with the notion that the emission can be used to characterize the atmospheric chemistry from secondary eclipse observations. Absorption features due to CH_4, CO, and H_2O would be nonexistent or extremely weak. Observations at other orbital phases would then take on additional importance.

Given the significant spectral differences between our model and radiative-equilibrium models, it is clear that more work in this area is certainly warranted. We note that blackbody-like hot Jupiter emission can simultaneously explain all observations to date. First is the secondary eclipse observation at 24 μm by Deming et al. (2005), a clear detection. Second is the very low flux ratio upper limit in L′ band by Deming et al. (2006b). Third is the 2.3 μm relative flux observation of Richardson et al. (2003a), which most one-dimensional models cannot fit (Seager et al. 2005). Fourth is the set of observations of TrES-1 by Charbonneau et al. (2005), who found an infrared spectral slope from 4.5 to 8 μm that was redder than that found by most one-dimensional models (Fortney et al. 2005; Barman et al. 2005). Additional observations of these planets, especially in the *Spitzer* 3.6 μm band, which catches much of the predicted 4 μm flux peak, would strengthen or refute this argument and provide a critical test for the CS06 dynamical simulation. Deming et al. (2006b) posited, perhaps with a wink, that a blackbody-like spectrum would be more consistent with observations to date than any published hot Jupiter model. Due to the dynamically altered temperature structure of the atmosphere of HD 209458b, we find that this could be the reality.

REFERENCES

Anders, E., & Grevesse, N. 1989, Geochim. Cosmochim. Acta, 53, 197
Barman, T. S., Hauschildt, P. H., & Allard, F. 2005, ApJ, 632, 1132
Bézard, B., Lellouch, E., Strobel, D., Maillard, J.-P., & Drossart, P. 2002, Icarus, 159, 95
Bouchy, F., et al. 2005, A&A, 444, L15
Brown, T. M., Charbonneau, D., Gilliland, R. L., Noyes, R. W., & Burrows, A. 2001, ApJ, 552, 699
Burkert, A., Lin, D. N. C., Bodenheimer, P. H., Jones, C. A., & Yorke, H. W. 2005, ApJ, 618, 512
Burrows, A., Hubeny, I., & Sudarsky, D. 2005, ApJ, 625, L135
Burrows, A., Sudarsky, D., & Hubeny, I. 2006, ApJ, 650, 1140
Charbonneau, D., Brown, T. M., Burrows, A., & Laughlin, G. 2006, in Proto-stars and Planets V, ed. Reipurth, D. Jewitt, & K. Keil (Tucson: Univ. Arizona Press) in press (astro-ph/0603376)
Charbonneau, D., Brown, T. M., Latham, D. W., & Mayor, M. 2000, ApJ, 529, L45
Charbonneau, D., Brown, T. M., Noyes, R. W., & Gilliland, R. L. 2002, ApJ, 568, 377
Charbonneau, D., Noyes, R. W., Korzennik, S. G., Nisenson, P., Jha, S., Vogt, S. S., & Kibrick, R. I. 1999, ApJ, 522, L145

Charbonneau, D., et al. 2005, ApJ, 626, 523
Cho, J. Y.-K., Menou, K., Hansen, B. M. S., & Seager, S. 2003, ApJ, 587, L117
Collier Cameron, A., Horne, K., Penny, A., & Leigh, C. 2002, MNRAS, 330, 187
Cooper, C. S., & Showman, A. P. 2005, ApJ, 629, L45
———. 2006, ApJ, 649, 1048 (CS06)
Deming, D., Harrington, J., Seager, S., & Richardson, L. J. 2006a, ApJ, 644, 560
Deming, D., Richardson, L. J., Seager, S., & Harrington, J. 2006b, in Tenth Anniversary of 51 Peg-b: Status of and Prospects for Hot Jupiter Studies, ed. L. Arnold, F. Bouchy, & C. Moutou (Paris: Frontier Group), 218
Deming, D., Seager, S., Richardson, L. J., & Harrington, J. 2005, Nature, 434, 740
Fegley, B., & Prinn, R. G. 1985, ApJ, 299, 1067
Fegley, B. J., & Lodders, K. 1994, Icarus, 110, 117
———. 1996, ApJ, 472, L37
Fortney, J. J., Marley, M. S., Lodders, K., Saumon, D., & Freedman, R. 2005, ApJ, 627, L69
Fortney, J. J., Saumon, D., Marley, M. S., Lodders, K., & Freedman, R. S. 2006, ApJ, 642, 495

Goody, R., West, R., Chen, L., & Crisp, D. 1989, J. Quant. Spectrosc. Radiat. Transfer, 42, 539

Griffith, C. A., & Yelle, R. V. 1999, ApJ, 519, L85

Henry, G. W., Marcy, G. W., Butler, R. P., & Vogt, S. S. 2000, ApJ, 529, L41

Holton, J. R. 1992, An Introduction to Dynamic Meteorology (3rd ed.; San Diego: Academic)

Iro, N., Bezard, B., & Guillot, T. 2005, A&A, 436, 719

Kalnay, E. 2002, Atmospheric Modeling, Data Assimilation and Predictability (Cambridge: Cambridge Univ. Press)

Kurucz, R. 1993, CD-ROM 13, ATLAS9 Stellar Atmosphere Programs and 2 km/s Grid (Cambridge: SAO)

Leigh, C., Collier Cameron, A., Udry, S., Donati, J.-F., Horne, K., James, D., & Penny, A. 2003, MNRAS, 346, L16

Liang, M., Parkinson, C. D., Lee, A. Y.-T., Yung, Y. L., & Seager, S. 2003, ApJ, 596, L247

Liang, M., Seager, S., Parkinson, C. D., Lee, A. Y.-T., & Yung, Y. L. 2004, ApJ, 605, L61

Lodders, K. 2002, ApJ, 577, 974

———. 2003, ApJ, 591, 1220

Lodders, K., & Fegley, B. 1998, The Planetary Scientist's Companion (New York: Oxford Univ. Press)

———. 2002, Icarus, 155, 393

Marley, M. S., Fortney, J., Seager, S., & Barman, T. 2006, in Protostars and Planets V, ed. B. Reipurth, D. Jewitt, & K. Keil (Tucson: Univ. Arizona Press) in press (astro-ph/0602468)

Noll, K. S., Geballe, T. R., & Marley, M. S. 1997, ApJ, 489, L87

Prinn, R. G., & Barshay, S. S. 1977, Science, 198, 1031

Richardson, L. J., Deming, D., & Seager, S. 2003a, ApJ, 597, 581

Richardson, L. J., Deming, D., Wiedemann, G., Goukenleuque, C., Steyert, D., Harrington, J., & Esposito, L. W. 2003b, ApJ, 584, 1053

Richardson, L. J., Harrington, J., Seager, S., & Deming, D. 2006, ApJ, 649, 1043

Saumon, D., Geballe, T. R., Leggett, S. K., Marley, M. S., Freedman, R. S., Lodders, K., Fegley, B., & Sengupta, S. K. 2000, ApJ, 541, 374

Saumon, D., Marley, M. S., Cushing, M. C., Leggett, S. K., Roellig, T. L., Lodders, K., & Freedman, R. S. 2006, ApJ, 647, 552

Saumon, D., Marley, M. S., Lodders, K., & Freedman, R. S. 2003, in Proc. IAU Symp. 211, Brown Dwarfs, ed. E. Martin (San Francisco: ASP), 345

Seager, S., Richardson, L. J., Hansen, B. M. S., Menou, K., Cho, J. Y.-K., & Deming, D. 2005, ApJ, 632, 1122

Seager, S., & Sasselov, D. D. 1998, ApJ, 502, L157

Showman, A. P., & Cooper, C. S. 2006, in Tenth Anniversary of 51 Peg-b: Status of and Prospects for Hot Jupiter Studies, ed. L. Arnold, F. Bouchy, & C. Moutou (Paris: Frontier Group), 242

Showman, A. P., & Guillot, T. 2002, A&A, 385, 166

Snellen, I. A. G. 2005, MNRAS, 363, 211

Suarez, M. J., & Takacs, L. L., ed. 1995, Documentation of the Aries/GEOS Dynamical Core Version 2 (NASA Tech. Memo 104606)

Toon, O. B., McKay, C. P., Ackerman, T. P., & Santhanam, K. 1989, J. Geophys. Res., 94, 16287

Visscher, C., & Fegley, B. J. 2005, ApJ, 623, 1221

———. 2006, ApJ, 648, 1181

Williams, P. K. G., Charbonneau, D., Cooper, C. S., Showman, A. P., & Fortney, J. J. 2006, ApJ, 649, 1020

Yung, Y. L., Drew, W. A., Pinto, J. P., & Friedl, R. R. 1988, Icarus, 73, 516